Sensors and Actuators A 169 (2011) 352–361

Contents lists available at ScienceDirect

Sensors and Actuators A: Physical

journal homepage: www.elsevier.com/locate/sna

Configuration analysis of sensing element for photonic crystal based NEMS cantilever using dual nano-ring resonator

Bo Li [a], Fu-Li Hsiao [a,b], Chengkuo Lee [a,*]

[a] Department of Electrical and Computer Engineering, National University of Singapore, 4 Engineering Drive 3, Singapore 117576, Singapore
[b] Institute of Photonics, National Changhua University of Education, No. 1, Jin-De Road, Changhua City 500, Taiwan, ROC

ARTICLE INFO

Article history:
Available online 17 March 2011

Keywords:
NEMS
Photonic crystal resonator
Nano-ring
Nanomechanical sensor
Microcantilever

ABSTRACT

Photonic crystal (PhC) based channel drop filters including two hexagonal rings in a two dimensional (2-D) photonic crystal silicon slab of hexagonal lattice are integrated on microcantilevers for nanoelectromechanical systems (NEMS) sensor applications. The proposed two hexagonal rings are named as dual nano-ring (DNR) resonator. The sensing characteristics of dual nano-ring (DNR) resonator at various positions adjacent to the junction of the microcantilever and the substrate are investigated. The derived quality factors is over 3000, and the minimum detectable force can be as small as 7.58 nN. Moreover, the continuous wave field distribution modeling is deployed to explain the origins of resonant mechanisms occurred in deformed DNR resonator under various applied forces.

1. Introduction

Over the past decade, the advent of micro- and nanotechnology has expedited the miniaturization of biochemical sensors, resulting in devices with an analytical performance better than their predecessors. The continuous effort in the miniaturization has been driven by the growing demands and interests in lab-on-a-chip (LoC) kind of devices from the biological and medical community. The goal of miniaturized LoC is a fully completed analytical and diagnostic system containing sample-loading, delivery, preparation, and rapid-detection components. The development of cantilever-based sensors for biochemical studies and clinical applications has been proven cantilever as a fundamental sensor platform [1,2]. The key feature distinguishing cantilever itself from other sensors is its high sensitivity to stress and strain, i.e., the beam deflection. To get rid of bulky displacement measurement unit which is prevailingly adopted in the commercial atomic force microscopy (AFM) systems, unique sensing mechanisms base on microelectromechanical systems (MEMS) technologies have been proposed, for example, the piezoresistive [3,4], the piezoelectric [5–10] and the capacitive [11] have been investigated extensively. It is a favorable approach for realization of multiple cantilever sensors by integrating nanometer scale sensing elements such that an array of cantilever sensors could be made in a very small form factor. Combining photonic crystal (PhC) waveguides and PhC resonators in an individual cantilever as the sensing element has been proposed as an intriguing solution for nanobiosensors of next generation [12–14]. Micro-ring based resonator has already been reported as a good candidate to achieve channel drop effect and those filters will be adapted in optical communications systems [15–18] and bio-particles detection [19]. Suspended silicon cantilevers and/or diaphragm integrated with PhC nanocavity based optical resonator has been investigated as a nanoelelctromechanical system (NEMS) sensor [12,20–22]. The output resonant wavelength is sensitive to the shape of air holes and defect length of the nanocavity resonator. When a strain is introduced by external force to the nanocavity resonator of a pair of two-holes separated by a point defect, the resonant wavelength and shift of output resonant wavelength can be measured as the function of parameters, like displacement, strain or force. Later on, this NEMS cantilever sensor has been characterized in terms of operation in air and water environment [14]. Rather linear relationship is derived for strain and resonant wavelength shift. The minimum detectable strain and force load are observed as 0.0136% and 0.046 μN for a 50 μm long and 15 μm wide cantilever, respectively [13].

In this article, we investigate NEMS cantilever sensors based on dual-nano-ring (DNR) resonators as sensing element. The configuration and location of two types of DNR resonators are computationally evaluated with respect to the sensing characteristics. The contributing factors of resonant modes of deformed DNR to the resulted resonant peak wavelength are explored.

2. Design, operation mechanism and modeling approach

PhC based ring resonator provides ultra-low bending loss due to very well light confinement. It offers good alternative of ultra-compact resonators with high quality factors (Q-factors) and high

* Corresponding author. Tel.: +65 6516 5865; fax: +65 6779 1103.
E-mail address: elelc@nus.edu.sg (C. Lee).

0924-4247/$ – see front matter © 2011 Elsevier B.V. All rights reserved.
doi:10.1016/j.sna.2011.03.020

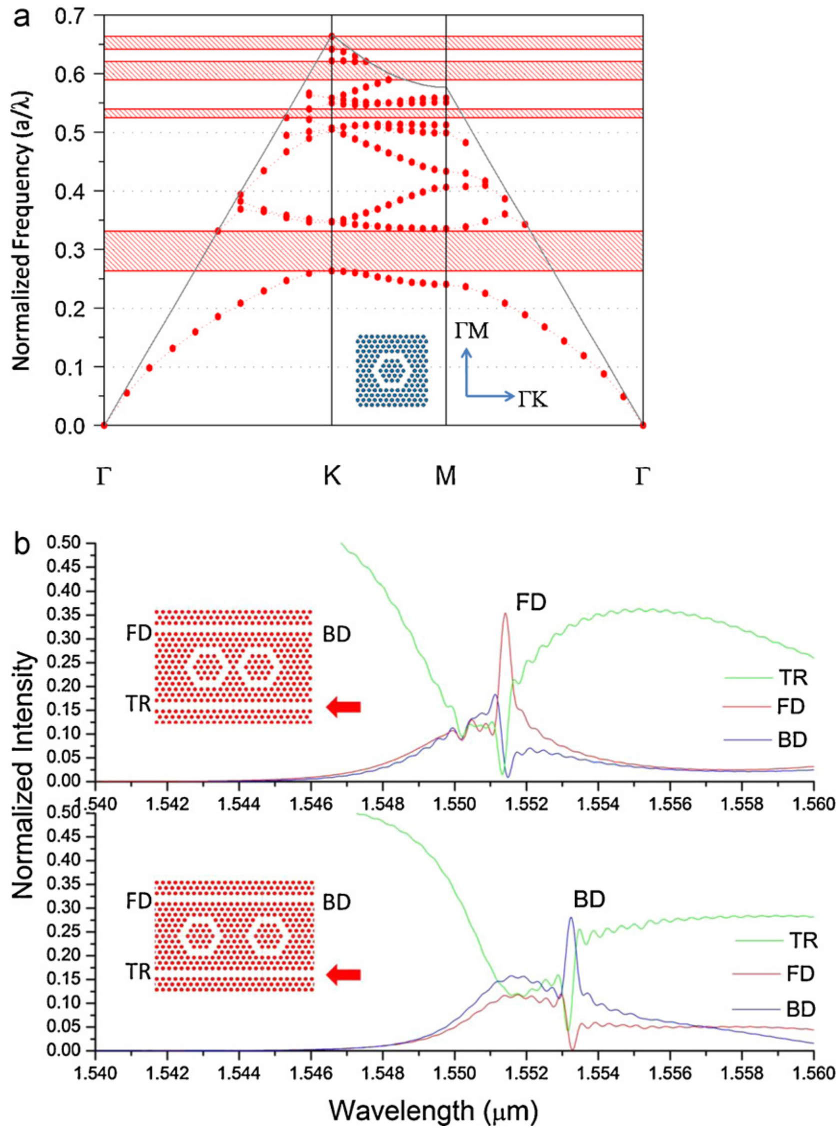

Fig. 1. (a) Band structure of the PhCs structure of hexagonal lattice. (b) Spectra of ports FD, BD and TR for 1 hole and 4 holes separation DNR channel drop filter.

wavelength selectivity. Kitamura et al. reported that the cavity modes obtained by plane wave expansion (PWE) method in PhC slab structure are in good agreement with the measured results [23]. By using this PWE method, the band gap structure of a 220 nm silicon PhCs slab of hexagonal lattice of air holes is derived, i.e., a case of air/220 nm-Si/air slab. According to the derived band gap map as shown in Fig. 1(a), the ratio between the radius of air holes (r) and lattice constant (a) is selected as 0.292, which is the middle of the band gap. The normalized frequency range of first photonic band gap extends from 0.26 to 0.33 in TM polarization electromagnetic wave, i.e., the magnetic field parallel to the surface of silicon slab. The corresponding directions of ΓM and ΓK with respect to hexagonal lattice are indicated in the inset of Fig. 1(a). The corresponding band gap wavelength range extends from 1.242 μm to 1.577 μm. A combinational approach of the 2-D finite-difference time-domain (FDTD) method and the effective refractive index (ERI) approximation was deployed to calculate and predict the performance of channel drop filter and the filed distribution of resonant mode in this study. Qiu reported a good agreement between the data derived by this combinational approach and full vector three dimensional (3-D) FDTD method [24]. Furthermore, experimental data have been predicted well by this combinational approach by the other groups as well [25,26].

As shown in Fig. 1(b), the hexagonal nano-rings and the waveguide are formed by removing the air holes in the PhC trace and the ERI of the 220 nm Si slab is derived as 2.7967 in the simulation. From the inset of Fig. 1(b), the light input port of the PhC DNR resonator is denoted by a red arrow and the other three ports are named as transmission (TR), forward drop (FD) and backward drop (BD), respectively. For the spectra intensity plot, TR, FD and BD ports are shown as green, red and blue curves, respectively. For DNR resonator with 1-hole separation between the rings, shown in the top of Fig. 1(b), resonant peak at 1551.41 nm is observed at the FD port with Q-factors about 3800. The intensity of BD port is only 6% of the FD port. For DNR resonator with 4-holes separation between the rings, shown in the bottom of Fig. 1(b), resonant peak at 1553.59 nm is observed at the BD port with Q-factors about 3800. The intensity of FD port is only 8% of the BD port. Hence, these two designs of DNR resonators are good channel drop filters. (For interpretation of the references to colour in this text, the reader is referred to the web version of this article.)

Based on the channel drop mechanism of the PhC DNR resonators, the resonance behavior is ultra sensitive with the defor-

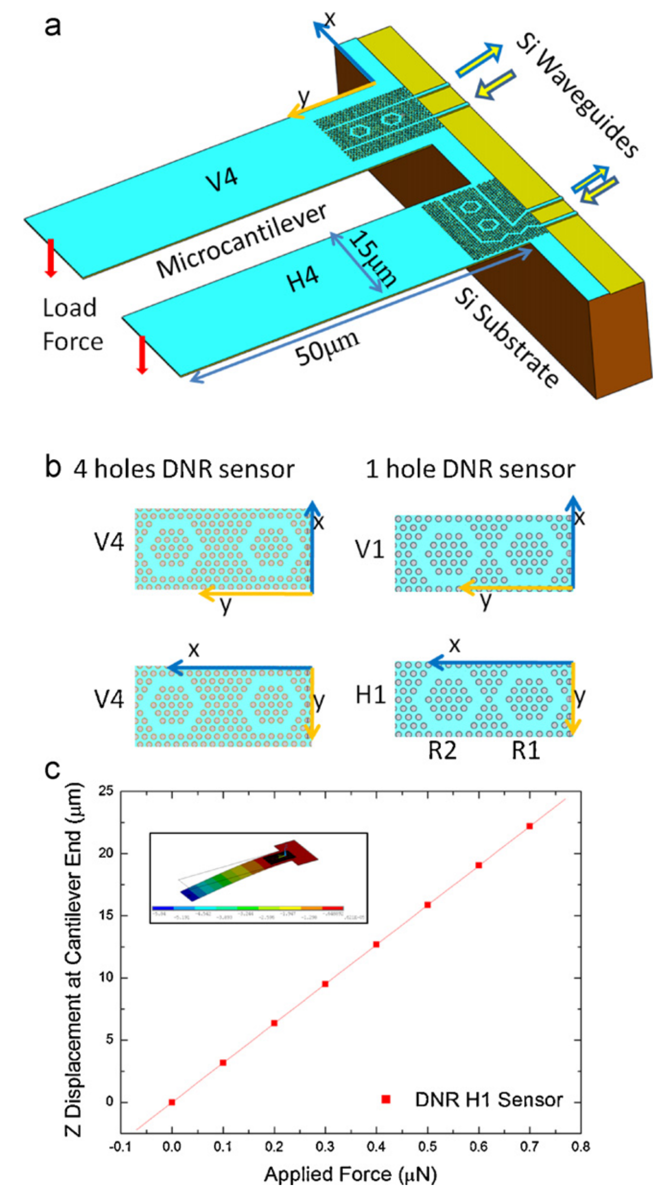

Fig. 2. (a) 3-D illustration of the device configuration of PhC cantilever sensor using hexagonal DNR resonator; (b) define the 4 types DNR cantilever sensors by varying the orientation of the DNR resonator; (c) *Z*-displacement at cantilever end versus applied force plot and the FEM simulation result.

mation of the PhC structure. Thus, it suggests that microcantilever integrated with a PhC DNR resonator is expected to be a good sensor for force and stain detection. The schematic of such force sensors are shown in Fig. 2, while the DNR resonator is aligned along the longitudinal direction (e.g. V4 type) or the lateral direction of the cantilever (e.g. H4 type), and is placed at the junction of a free-standing silicon cantilever and an edge of substrate. The cantilever with length and width of 50 μm and 15 μm can be patterned and released from the 220 nm thick silicon device layer of a SOI substrate. The lattice constant (a) of 410 nm and air hole radius (r) of 180 nm of the PhC slab of hexagonal lattice are deployed in modeling. Two hexagonal nano-rings are placed along the longitudinal or transversal direction of the cantilever, and are separated by some air-holes along their symmetric axis. The whole layout configuration including the lattice constant, a, air hole radius, r, and the air-hole separation between waveguides and rings has been optimized in order to achieve resonant peak with higher Q-factors. 4 types of microcantilever sensors are characterized in this study, i.e., the DNR resonator is placed longitudinally (*Y* direction) and transversely (*X* direction) against to the cantilever beam with regard to two types of hole-separation, e.g. 1-hole and 4-holes cases. As shown in Fig. 2(b). The microcantilever sensors with DNR resonator of 4-holes separation for longitudinal and transverse layout arrangement are named as V4 and H4, respectively, while the equivalent layout arrangement for microcantilever sensors of 1-hole separation are named as V1 and H1 accordingly.

In the applications, when an external force is applied on the cantilever free-end, the strain at the junction is created. Such strain is in linear proportion to the applied force. More precisely, the vertical displacement (*Z*-displacement) at different positions along the longitudinal direction of the cantilever is gradually increased as the position moves to the cantilever free-end under an applied force. Finite-element analysis (FEA) is deployed to obtain the deformation data of holes among PhC air-hole array of the sensing element region under various force loads which are applied at the centre point of the cantilever free-end (Fig. 2(c), inset). The Young's modulus and Poisson's ratio of Si used in FEA simulation are 130 GPa and 0.3 respectively. As a result, the location of DNR resonators leads to different strain and deformation. The bending profile of cantilevers has linear relations with the applied force. Fig. 2(c) illustrates the well-defined linear relationship of the *Z* direction displacement at cantilever end and the applied force of the H1 sensor. In the following discussion, we investigate the resonant wavelength and resonant wavelength shift with respect to the applied force mainly, while we can foresee the same trend of curves could be derived for curves of resonant wavelength versus *Z*-direction displacement, or resonant wavelength shift versus *Z*-direction displacement. We further apply numerical 2-D FDTD method with ERI method to simulate the propagation of the electromagnetic waves in the deformed PhC DNR resonator structure in the present of various applied force loads. We expect the resonant peak at active port will vary according to the strain of DNR resonator. In our previous study [27], we realized that the shape change of air-holes among the deformed PhC nanocavity resonator structure does not affect on the output resonant behavior. More importantly, the relative position shifts of these air-holes among the deformed PhC nanocavity resonator structure play a major role in contribution to the resonant behavior. Thus we record the position of holes in the deformed region of the whole sensing element of air-hole array of the microcantilever under force load according to the FEA results, and conduct the 2-D FDTD modeling based on the layout of such deformed DNR resonators.

3. Sensor characteristics

As shown in Fig. 1(b), two different types of channel drop ports are reported for the DNR resonator, i.e., FD port channel drop of 1 hole separation and BD port channel drop of 4 holes separation, respectively.

3.1. DNR resonator with 4-holes separation

Fig. 3 shows the resonant wavelength peak for V4 and H4 sensors derived at the BD port under different force loads with a step of 0.1 μN. The resonant peak which is located at 1553.59 nm with Q-factor of about 3800 is referred as the no-load case. As force increases, both sensors show a red shift of the resonant wavelength and demonstrate well-defined resonant peak within the force range of 0.4 μN. However, in the case of the V4 sensor, the intensity of resonant peak at BD port becomes relatively weak when the force reaches to 0.5 μN. It is suggested by a mechanism that the channel drop effect becomes weak such that limited amount of light coupled to the BD terminal via the DNR and most of the pumped energy goes

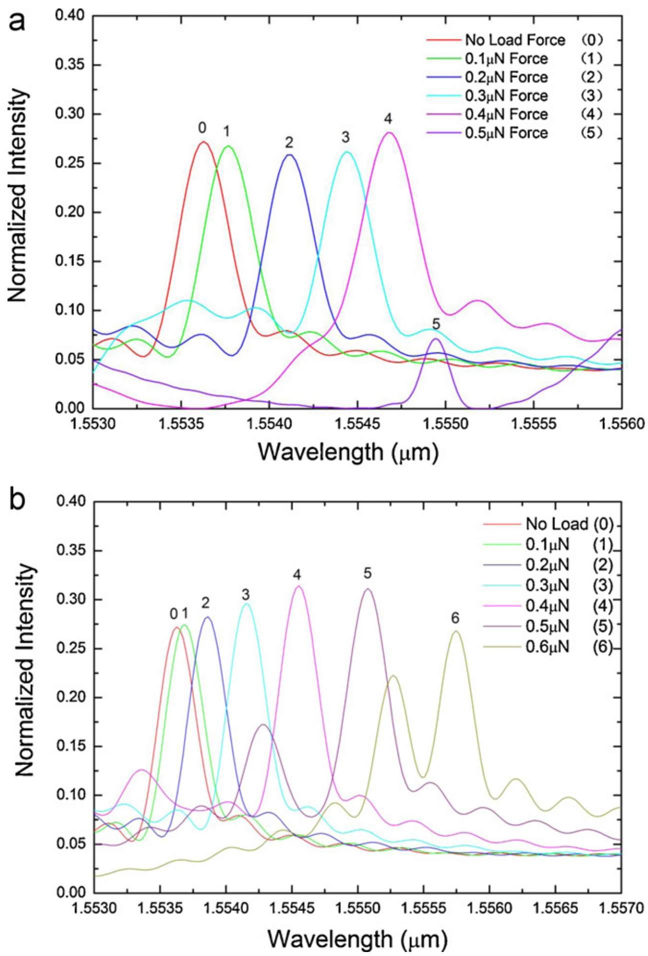

Fig. 3. Resonant wavelength peak with various load force (a) V4 sensor and (b) H4 sensors.

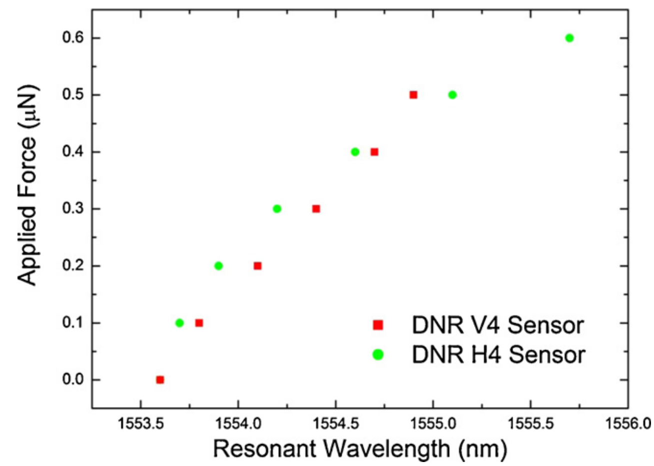

Fig. 4. Resonant wavelength as functions of applied force for V4 and H4 cantilever sensors.

to the TR port. In other words, the resonance of the DNR is slightly deviated while the DNR resonator experiencing the large deformation. Thus the coupling becomes worse. In the H4 sensor case, both rings of DNR experience the same amount of deformation due to the cantilever bending, since the two rings are placed in transverse direction of the cantilever. A minor peak of shorter wavelength except to the major peak is observed for H4 sensor under force loads of 0.5 μN and 0.6 μN, because the deformed ring shape brings extra coupled energy which matches another resonance at BD port as well.

Fig. 4 illustrates the relationship of the wavelength of resonant peak at BD port versus applied force of the both sensors. Linear relationship is observed for the V4 sensor, while the slope is derived as 2.7 nm/μN. It is suggested that the minimum detectable force will be 37 nN, if we have the wavelength resolution of 0.1 nm in the testing setup. However, a 2nd-order polynomial fitting curve has good agreement with the derived data point in the case of H4 sensor. From the 2nd-order polynomial fitting curve, we get different sensitivity in different range of force loads for various applications. More specifically, the slope of the fitting curve for force less than 0.1 μN is derived as 1 nm/μN, while such slope is 6 nm/μN in the force region of 0.5–0.6 μN. As a result, the minimum detectable force is calculated as 100 nN and 16.7 nN in these two regions, respectively.

3.2. DNR resonator with 1-hole separation

Fig. 5 shows the resonant wavelength peak for V1 and H1 sensors derived at the FD port under different force loads in a step of 0.1 μN. Different from the 4-holes separation case, the resonant wavelength of the no load case locates at the 1551.41 nm. The resonant peaks shift to the higher wavelength range when the loaded force increases for both V1 and H1 sensors. However, the Q-factor of the resonant peak for V1 sensor drops dramatically as force increases, from over 3000 of no load case to 873 of 0.5 μN applied-force case. The output intensity also drops as force increases. Thus, these imply

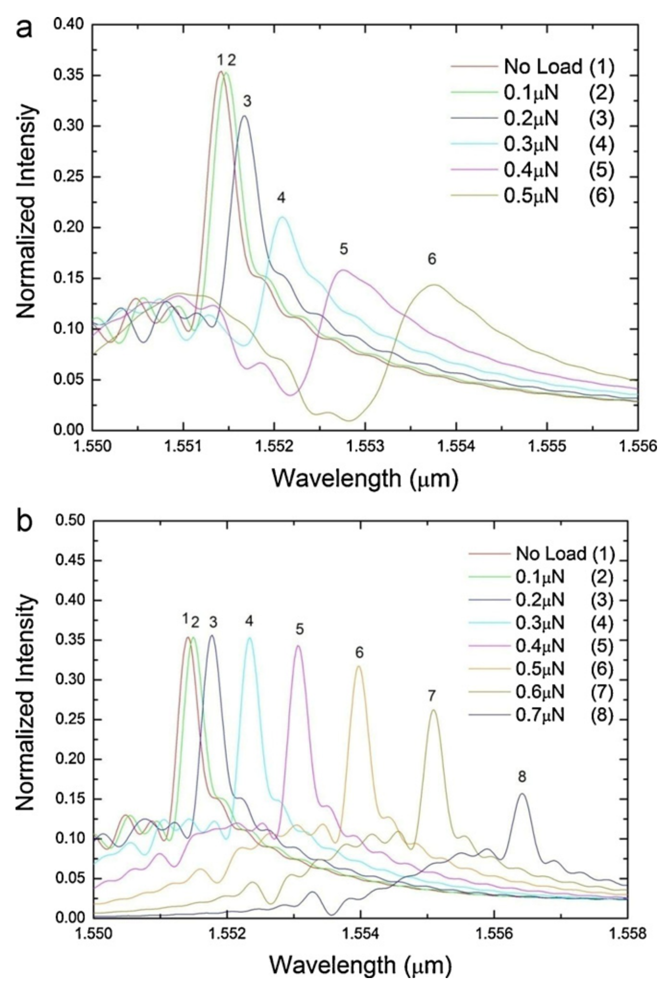

Fig. 5. Resonant wavelength peak with various load force (a) V1 sensor and (b) H1 sensors.

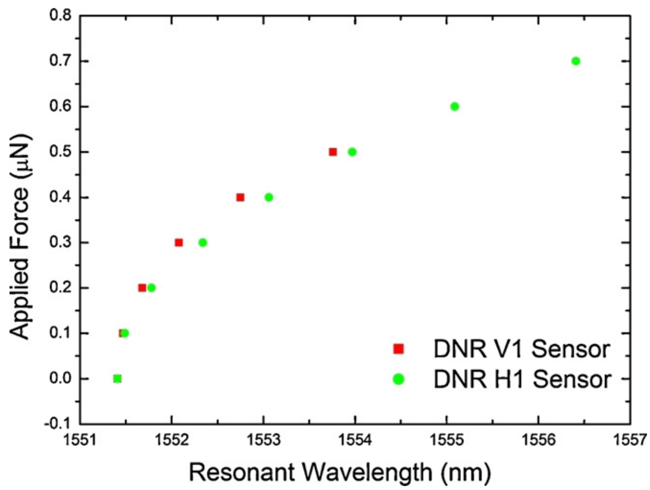

Fig. 6. Resonant wavelength as functions of applied force for V1 and H1 cantilever sensors.

that the deformation of V1 DNR resonator changes the resonant properties as well as the light confinement of the resonator. Hence, the sensible range of the V1 would be the smallest among all the proposed sensors. On the other hand, H1 resonator shows much better Q-factor and output intensity in large force sensing range. The resonant peaks lose its comparable intensity until the applied force reach 0.7 μN which is the best result among all the 4 types of microcantilever sensors.

The curves of resonant wavelength versus the applied force for V1 and H1 sensors are shown in Fig. 6. Both the sensors show the same 2^{nd}-order polynomial trend of relationship of the resonant wavelength and the applied force. In contrast of Fig. 4, the data points of V1 have close location with the H1, at which it could imply that the resonance mechanism and deformation influences are similar for these two kinds of 1-hole separation DNR resonator. Moreover, similar with the H4 case, 2^{nd}-order polynomial relationship of resonant wavelength and the applied force indicate different sensitivity in different force-load range. Therefore, the minimum detectable force of V1 can be derived as 167 nN and 9.9 nN in the two regions, respectively. The minimum detectable force of H1 can be derived as 125 nN and 7.58 nN in these two regions, respectively.

4. Study of resonant modes under deformation

To further conduct the optimization of the DNR microcantilever sensors, the origin of resonant wavelength shift and the corresponding behaviors of wavelength shift versus the force loads are interested to us. Thus, continuous wave field distribution has been established on DNR resonator under the various applied force within the detectable force range for the four cantilever sensors. Fig. 7 shows resonator structure and frames of the resonator magnetic field distribution in the steady state condition. The TM mode Gaussian beam centered at the resonant wavelength launches into the resonator from the bottom right input port of each structure. We define the right hand side ring as R1 and the left hand side ring as R2 respectively. The input light beam comes from the bottom right side and travels along the input waveguide and will excite the DNR region. The DNR then can couple the light energy of certain wavelength to the output waveguide. For the simplicity of the descriptions, we grouped and labeled some of the air holes, as shown in Fig. 7(a) and (b). Air holes in group A represent the outer level of the nano-rings. Air holes in group B represent the inner level of the nano-rings. Group C contain the air holes which connect the two rings. Air holes in group D form the coupling path of the ring to the waveguide. Fig. 7(c) and (e) illustrates the field distribution of DNR cantilever sensors of 4-holes separation under no load condition at different modes. Group C air holes show strong field energy which implies that there is coupling effect between the two rings. High level of energy exchange in the group C holes between the DNR indicates that the two rings are not working independently of each other. Light comes from the input waveguide will travel and resonant within the two rings first before couples to the BD port at the output waveguide. More specifically, the 4-air-holes in the group C form a line which plays an important role in the DNR resonance. Group A and B are close to the nano-rings region so that field disperses to those air holes. Air holes of group A have alternative color changes starting from dark blue at A1 in odd mode. The dark red and dark blue represent the maximum and minimum of the field. Similarly, Air holes of group B also have the alternative color changes but starting from dark red at B1 in the odd mode. Waves couple from rings to the waveguide via A1 and group D air holes. However, because of the deconstructive interference, most of the light goes to the BD port and fulfill the channel drop effect. Moreover, the two rings are always in the same phase, and light energy strength changes periodically and simultaneously. In the even mode, Fig. 7(e), all the air holes exchange their field strength but stay there distribution configurations. (For interpretation of the references to colour in this text, the reader is referred to the web version of this article.)

For Fig. 7(d) and (f), field distributions of the DNR microcantilever sensor of 1-hole separation under no load condition are illustrated. Different from the 4-holes separation DNR case, there is no coupling between the two rings, i.e., air holes of group C have blank zero field strength. More clearly, the two rings are working independently. However, similar with the 4-holes separation case, air holes of group A and group B in the 1-hole separation case have alternative color changes with starting from dark red and dark blue in the odd mode case respectively. For the even mode, exchange of the field strength happens on all of the air hole but without configuration changes. In general, equal strength of energy distributes in both rings and then couples into the output waveguide. The FD port is activated by the deconstructive interference of the signal out from air holes of the group D. (For interpretation of the references to colour in this text, the reader is referred to the web version of this article.)

When force applied on the microcantilever, the PhCs structure deformation is introduced by the bending of the Si beam and therefore the field distribution is differ from the no load case. Fig. 8(a–h) illustrates gradually change of the 4-holes separation DNR cantilever sensors under no load condition, 0.5 μN load of V4 DNR sensor and 0.6 μN load of H4 DNR sensor over half period. During the half period, the field configuration changes from the odd mode to the even mode and the rest half period is exactly symmetry of the previous one but change from even mode to odd mode. For V4 sensor under 0.5 μN case, two rings lost their symmetrical shape, comparing with the no load case, due to their different locations on the Si cantilever beam. Hence, as shown in Fig. 8, the symmetry of the DNR resonance has been destroyed and most of time only R1 is under strong resonance condition but R2 plays minor roles. However, energy exchange still happens in the air holes of group C, some resonant energy stays inside R2. On the other hand, when the DNR placed transversely on the Si cantilever, i.e., the H4 case, two rings experience the same amount of deformation. Thus, the field distribution graph of H4 are quite similar with the no load condition at each time interval. However, in the (f) set of Fig. 8, H4 sensor does not show the symmetry as the mode period is changed.

Fig. 9(a–h) illustrates gradually change of field distribution of 1-hole separation DNR cantilever sensor under no load condition, 0.5 μN load of V1 sensor and 0.7 μN load of H1 case over half period. For 1-hole separation DNR sensor, due to no coupling between the two rings, two rings do not always change the strength simulta-

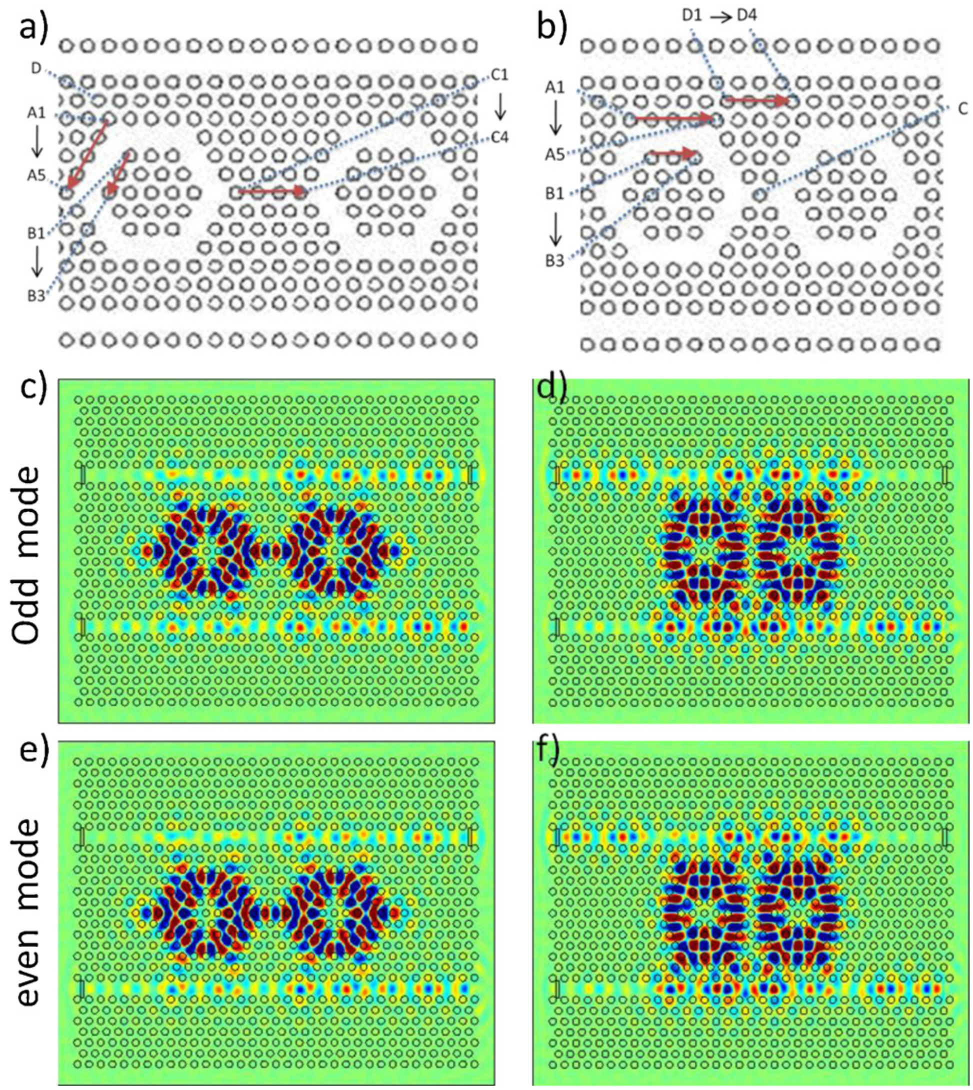

Fig. 7. Images of field distribution configuration for DNR resonators at steady state no load condition. (a) Specific definition of resonant air holes for 4-holes separation resonator. (b) Specific definition of resonant air holes for 1-hole separation resonator. (c) Odd mode of light resonance in 4-holes separation resonator. (d) Odd mode of light resonance in 1-hole separation resonator. (e) Even mode of light resonance in 4-holes separation resonator. (f) Even mode of light resonance in 1-hole separation resonator.

neously. As shown of Fig. 9(d) and (f), R1 and R2 are separately dominant of the resonance. For V1 sensor under 0.5 μN load case, R2 is always the ring with high resonance, while R1 has very weak resonance. Hence, rings' shape-mismatch results in the asymmetry of ring resonance. Moreover, since there is no coupling between the two rings, energy inside R1 is much lower than the R2. The energy lost here results in the low Q-factor in the output spectra. For H1 sensor under 0.8 μN load case, the field distribution is similar to the no load case because the two rings have exactly the same deformation data. However, the field at the top and bottom of the DNR shoulder shows differences since the large deformation bring the asymmetry of the DNR about the horizontal line of Fig. 9(a) and (h).

In order to fully understand the contribution of the DNR in the PhC sensors, we conduct another simulation for the longitudinally placed DNR but only single ring appears on the cantilever and all the other parts of resonator are located on the substrate. More clearly, only single hole experiences the deformation and other parts do not. Thus, we eliminate the ring shape deformation effect and only consider the contribution of the ring separation air holes and the second ring. Hence, together with the single nano-ring (SNR) resonator cantilever sensor, three types of cantilever sensors with exactly the same deformation data of the resonator are simulated and plotted in Fig. 10. Since we have demonstrated in Fig. 2(c) that the cantilever deformation profile has good linear relationship with the applied force, hence we can predict that the deformation versus the curve resonance wavelength shift plot would have the same shape with the applied force versus resonance wavelength shift plot, i.e., Fig. 10. From the fitting curve of each type of sensor's relationship of resonant wavelength shift and the applied force, it is obvious that the SNR sensor shows a strong 2^{nd}-order polynomial fitting curve, DNR 4-holes sensor shows a linear fitting curve and the DNR 1-hole sensor shows linear for small load force but change to weak 2^{nd}-order polynomial when force become large. It clearly shows when ring shape deformation plays main roles in the PhC resonator sensor mechanism, the sensor characteristic show a 2^{nd}-order polynomial relationship; on the other hand, when the separation become larger than the equivalent size of the two rings, linear relationship of the sensor characteristic is observed.

In summary, the ring shape deformation and the change in the separation between two rings of DNR are considered as contributing effect of the sensor characteristic. Thus, we need to include ring shape deformation and strain of ring separation in account when we discuss the behavior of DNR sensor. The different relationship (linear and 2^{nd}-order polynomial) of the curves of resonant wave-

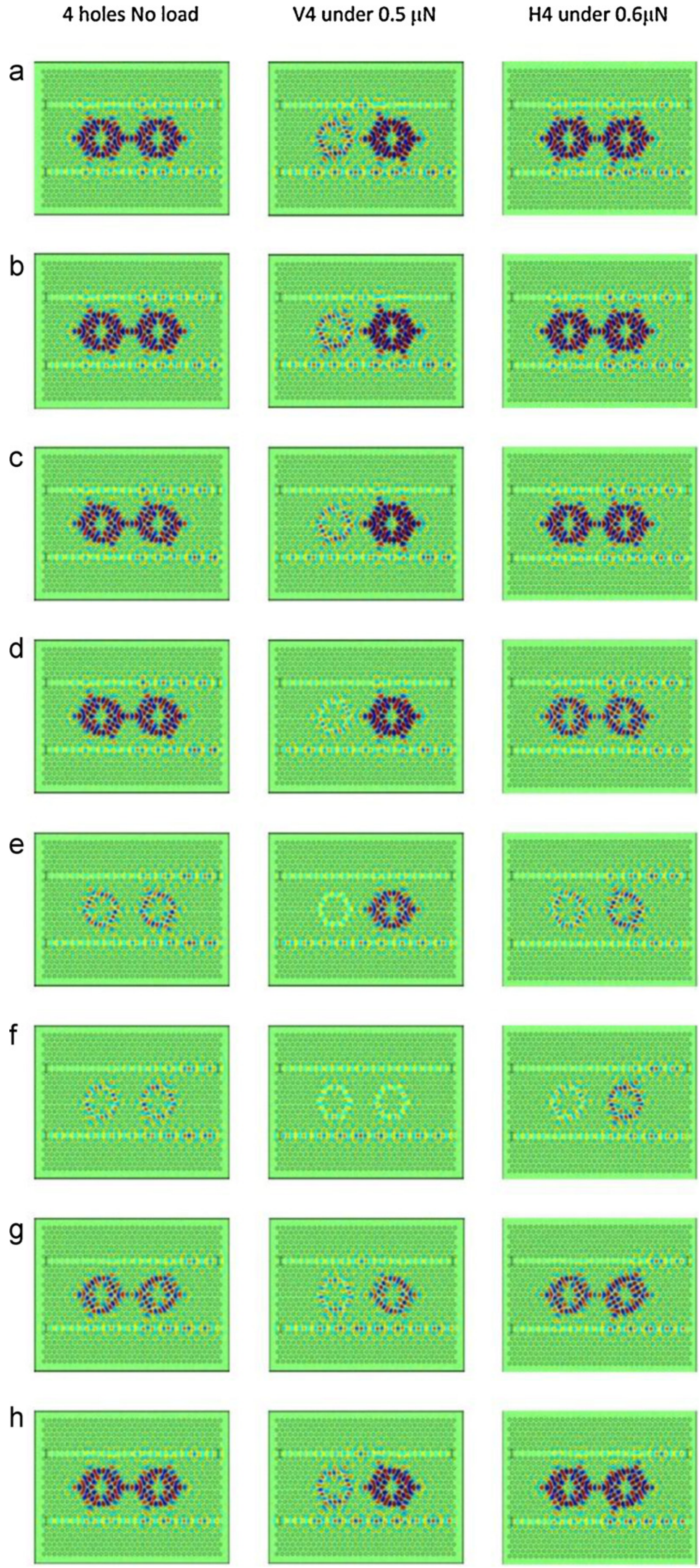

Fig. 8. Images of continuous wave field distribution of half cycle for 4 holes separation DNR resonator sensor under no load condition, V4 sensor under 0.5 μN load condition and H4 sensor under 0.6 μN load condition. (a)–(h), 1/16 cycle difference for adjacent two frames.

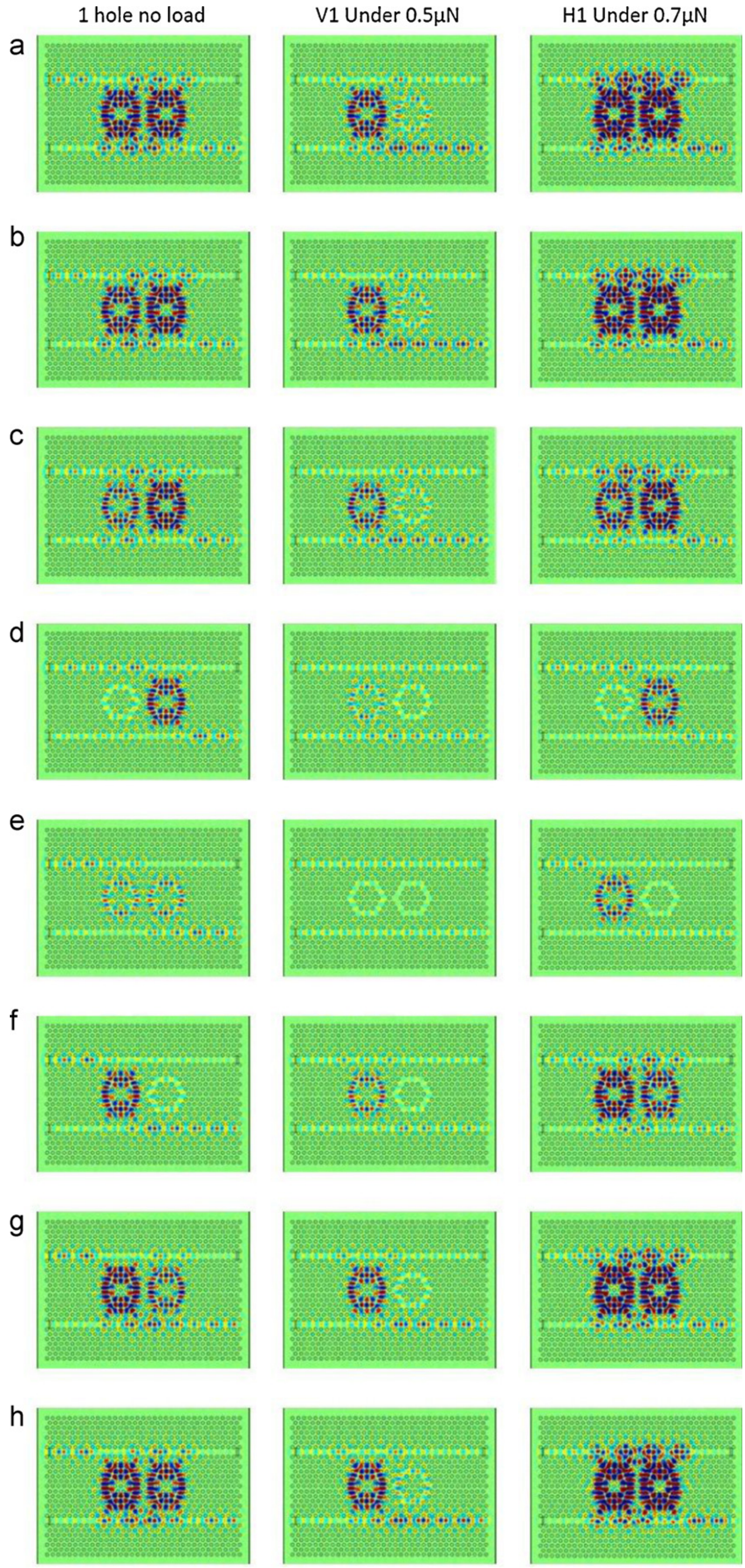

Fig. 9. Images of continuous wave field distribution of half cycle for 1 hole separation DNR resonator sensor under no load condition, V1 sensor under 0.5 μN load condition and H1 sensor under 0.7 μN load condition. (a)–(h), 1/16 cycle difference for adjacent two frames.

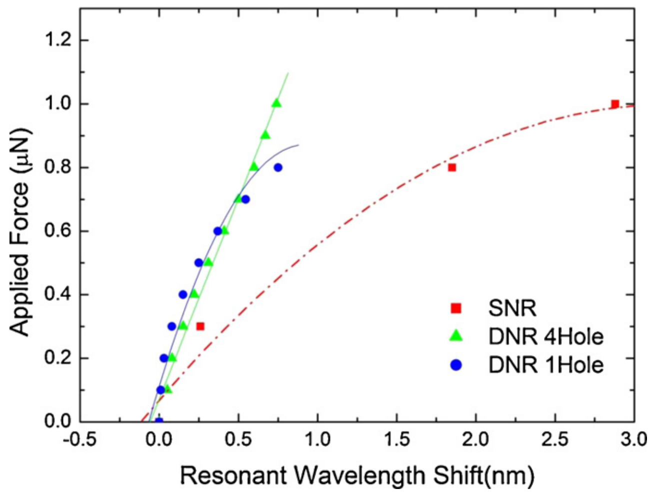

Fig. 10. Curve of resonant wavelength shift versus applied force for cantilever of SNR and shifted DNR 4 holes separation and 1 hole separation cantilever.

length versus the applied force is attributed to the deformation of rings. When rings are longitudinal placed, different ring shape deformation will reduce the ring coupling and the ring separation coupling will play the main role. Sufficient large strain is created in such ring separation in theV4 sensor, and a linear relationship is shown (Fig. 4). However, for the V1 case, since no coupling happens in the ring separation air hole from the beginning, ring separation deformation does not account into the contribution but the ring shape deformation does. Therefore, the 2^{nd}-order polynomial is observed for the V1 sensor, as shown in Fig. 6. On the other hand, we only consider the ring shape deformation in the transversely placed sensors, i.e., H4 and H1 sensors, due to the negligible change in the ring separation.

In addition, the Q-factors of the resonant peaks of transversely placed sensor (H1 and H4) are holding better compared with the data of longitudinally placed sensor (V1 and V4). The only problem is the minor peak appears when the force load is larger than 0.4 μN in the H4 sensor. But the major peak of longer wavelength can be easily recognized, we believe this factor would not affect on the sensor characteristics.

5. Conclusions

Microcantilevers using integrated photonic crystal (PhC) based channel drop filters, which contains two hexagonal nano-rings, i.e., dual-nano-ring (DNR) resonator, are proposed for nanoelectromechanical systems (NEMS) sensor applications. We investigate locations of DNR arranged longitudinal direction and transverse direction at various positions adjacent to the junction of the microcantilever and the substrate. The derived Q-factor of no force load case is over 3000. The minimum detectable force of microcantilever with DNR resonator of different configurations is characterized. Moreover, the continuous wave field distribution modeling is deployed to explain the origins of resonant mechanisms occurred in deformed DNR resonator under various applied forces.

Acknowledgements

This work was supported in research grants of University Research Fund R-263-000-475-112 at the National University of Singapore, and A*-STAR, SERC Grant No. 0921010049. Authors thank valuable advice from Prof. Aaron Danner and Prof. Gengchiau Liang. Authors also thank the technical support from staff at Computational Nanoelectronics & Nanodevices Lab., Microelectronics Lab., Centre for Integrated Circuit Failure Analysis & Reliability (CICFAR), and Centre for Optoelectronics of National University of Singapore.

References

[1] N.V. Lavrik, M.J. Sepaniak, P.G. Datskos, Cantilever transducers as a platform for chemical and biological sensors, Rev. Sci. Instrum. 75 (2004) 2229–2253.
[2] C. Ziegler, Cantilever-based biosensors, Anal. Bioanal. Chem. 379 (2004) 946–959.
[3] M. Tortonese, R.C. Barrett, C.F. Quate, Atomic resolution with an atomic force microscope using piezoresistive detection, Appl. Phys. Lett. 62 (1993) 834–836.
[4] P.A. Rasmussen, J. Thaysen, O. Hansen, S.C. Eriksen, A. Boisen, Optimised cantilever biosensor with piezoresistive read-out, Ultramicroscopy 97 (2003) 371–376.
[5] T. Itoh, C. Lee, T. Suga, Deflection detection and feedback actuation using a self-excited piezoelectric Pb (Zr, Ti)O_3 microcantilever for dynamic scanning force microscopy, Appl. Phys. Lett. 69 (1996) 2036–2038.
[6] C. Lee, T. Itoh, R. Maeda, T. Ohashi, T. Suga, Development of a piezoelectric self-excitation and self-detection mechanism of PZT microcantilevers for dynamic SFM in liquid, J. Vac. Sci. Technol. B 15 (1997) 1559–1563.
[7] J. Chu, T. Itoh, C. Lee, T. Suga, K. Watanabe, Frequency modulation detection high vacuum scanning force microscope with a Self-oscillating piezoelectric cantilever, J. Vac. Sci. Technol. B 15 (1997) 1647–1651.
[8] C. Lee, T. Itoh, T. Suga, Self-excited piezoelectric PZT microcantilevers for dynamic SFM-with inherent sensing and actuating capabilities, Sens. Actuators A 72 (1999) 179–188.
[9] W. Dong, X. Lu, M. Liu, Y. Cui, J. Wang, Measurement on the actuating and sensing capability of a PZT microcantilever, Meas. Sci. Technol. 18 (2007) 601–608.
[10] S. Shin, J.P. Kim, S.J. Sim, J. Lee, A multisized piezoelectric microcantilever biosensor array for the quantitative analysis of mass and surface stress, Appl. Phys. Lett. 93 (2008) 102902.
[11] J. Brugger, R.A. Buser, N.F. de Rooij, Micromachined atomic force microprobe with integrated capacitive readout, J. Micromech. Microeng. 2 (1992) 218–220.
[12] C. Lee, J. Thillaigovindan, C. Chen, X.T. Chen, Y. Chao, S. Tao, W. Xiang, A. Yu, H. Feng, G.Q. Lo, Si nanophotonics based cantilever sensor, Appl. Phys. Lett. 93 (2008) 113113.
[13] C. Lee, J. Thillaigovindan, Optical nanomechanical sensor using a silicon photonic crystals cantilever embedded with a nanocavity resonator, Appl. Opt. 48 (2009) 1797–1803.
[14] W. Xiang, C. Lee, Nanophotonics sensor based on microcantilever for chemical analysis, IEEE J. Sel. Top. Quant. Electron. 15 (2009) 1323–1326.
[15] A. Melloni, R. Costa, P. Monguzzi, M. Martinelli, Ring-resonator filters in silicon oxynitride technology for dense wavelength-division multiplexing systems, Opt. Lett. 28 (2003) 1567–1569.
[16] T. Barwicz, M.A. Popovic, P.T. Rakich, M.R. Watts, H.A. Haus, E.P. Ippen, H.I. Smith, Microring-reasonatorbased add-drop filters in SiN: fabrication and analysis, Opt. Express 12 (2004) 1437–1442.
[17] Z. Qiang, W. Zhou, R.A. Soref, Optical add-drop filters based on photonic crystal ring resonators, Opt. Express 15 (2007) 1823–1831.
[18] Z. Zhang, M. Qiu, Compact in-plane channel drop filter design using a single cavity with two degenerate modes in 2D photonic crystal slabs, Opt. Express 13 (2005) 2596–2604.
[19] F.-L. Hsiao, C. Lee, Nanophotonic biosensors using hexagonal nano-ring resonators – A computational study, SPIE J. of Micro/Nanolithography, MEMS, and MOEMS (JM3) 10 (2011) 013001.
[20] T.T. Mai, F.-L. Hsiao, C. Lee, W. Xiang, C.-C. Chen, W.K. Choi, Optimization and comparison of photonic crystal resonators for silicon microcantilever sensors, Sens. Actuators A 165 (2011) 16–25.
[21] B. Li, F.-L. Hsiao, C. Lee, Computational characterization of photonic crystal cantilever sensor using hexagonal dual-nano-ring based channel drop filter, IEEE Trans. Nanotechnol. (2011), doi:10.1109/TNANO.2010.2079942.
[22] B. Li, C. Lee, NEMS diaphragm sensors integrated with triple nano ring resonator, Sens. Actuators A: Phys. (2011), doi:10.1016/j.sna.2011.02.028.
[23] M. Kitamura, S. Iwamoto, Y. Arakawa, Enhanced light emission from an organic photonic crystal with a nanocavity, Appl. Phys. Lett. 87 (2005) 151119.
[24] M. Qiu, Effective index method for the heterostructure-slab-waveguides-based two-dimensional photonic crystals, Appl. Phys. Lett. 81 (2002) 1163.
[25] W. Zheng, M. Xing, G. Ren, S.G. Johnson, W. Zhou, W. Chen, L. Chen, Integration of a photonic crystal polarization beam splitter and waveguide bend, Opt. Express 17 (2009) 8657–8668.
[26] Y. Chassagneux, R. Colombelli, W. Maineults, S. Barbieri, S.P. Khanna, E.H. Linfield, A.G. Davies, Predictable surface emission patterns in terahertz photonic-crystal quantum cascade lasers, Opt. Express 17 (2009) 9492–9502.
[27] C. Lee, R. Radhakrishnan, C.-C. Chen, J. Li, J. Thillaigovindan, N. Balasubramanian, Design and Modeling of a Nanomechanical Sensor Using Silicon Photonic Crystal, IEEE J. Lightwave Technol. 26 (2008) 839–846.

Biographies

Bo Li received the B.Sc. degree from the Department of Electrical and Computer Engineering at the National University of Singapore in 2009. He is currently working toward his Ph.D. degree at the same university.

Fu-Li Hsiao received the B.S. degree in the Department of Physics of National Changhua University of Education, Taiwan, in 2002 and the Ph.D. degree in FEMTO-ST of University of Franche-Comte, France, and in Department of Optics and Photonics of National Central University, Taiwan, in 2008. He has been a post-doctoral research fellow in the Department of Electrical and Computer Engineering at Nation University of Singapore in 2008–2009. Currently he is an assistant profesoor in Institute of Photonics at National Changhua University of Education, Changhua City, Taiwan. He is also a visiting scholar the Department of Electrical and Computer Engineering at Nation University of Singapore now. His research interests include photonic crystals, phononic crystals and optical MEMS.

Chengkuo Lee (S'93–M'96) received the M.S. degree in materials science and engineering from National Tsing Hua University, Hsinchu, Taiwan, ROC, in 1991, the M.S. degree in industrial and system engineering from Rutgers University, New Brunswick, NJ, in 1993, and the Ph.D. degree in precision engineering from the University of Tokyo, Tokyo, Japan, in 1996. He worked as foreign researcher in the Nanometerscale Manufacturing Science Laboratory at the Research Centre for Advanced Science and Technology (RCAST) of the University of Tokyo from 1993 to 1996. He had also worked in the Mechanical Engineering Laboratory, AIST, MITI of Japan as a JST Research Fellow in 1996. Thereafter, he was a senior research staff member of Microsystems Laboratory, Industrial Technology Research Institute (ITRI), Hsinchu, Taiwan, ROC In September 1997, he joined the Metrodyne Microsystem Corporation, Hsinchu, Taiwan, ROC, and established the MEMS device division and the first micromachining fab for commercial purposes in Taiwan. He was the Manager of the MEMS device division between 1997 and 2000. He was an adjunct assistant professor in the Electro-physics Department of National Chiao Tung University, Taiwan, ROC in 1998, and an adjunct assistant professor in the Institute of Precision Engineering of the National Chung Hsing University, Taiwan, ROC, from 2001 to 2005. He co-founded Asia Pacific Microsystems, Inc. (APM) Hsinchu, Taiwan, ROC, in August 2001, and he became the Vice President of R&D, then later until the end of 2005, the VP of optical communication business unit and special assistant of CEO in charge of international business and technical marketing for MEMS foundry service at APM, Inc., one of the top 30 MEMS manufacturers in the world in 2004. From 2006 to 2009, he has been a senior member of technical staff at the Institute of Microelectronics (IME), A*Star, Singapore. He has been an assistant professor at the Dept. of Electrical and Computer Eng. of National University of Singapore, Singapore since December 2005. He is the co-author of a book in title of Advanced MEMS Packaging, McGraw-Hill, 2010. He has contributed more than 130 international conference papers and extended abstracts, 85 peer-reviewed international journal articles, and 9 US patents in MEMS, Nanophotonics and Nanotechnology fields. Dr. Lee is the member of the Materials Research Society (MRS), IEEE and the Institution of Electrical Engineers (IEE) Japan.